PHYSICAL REVIEW B **99**, 205422 (2019)

Disordered Si:P nanostructures as switches and wires for nanodevices

Amintor Dusko,[1,*] Belita Koiller,[2] and Caio Lewenkopf[1]
[1]*Instituto de Física, Universidade Federal Fluminense, 24210-346 Niterói, Rio de Janeiro, Brazil*
[2]*Instituto de Física, Universidade Federal do Rio de Janeiro, Caixa Postal 68528, 21941-972 Rio de Janeiro, Brazil*

(Received 1 February 2019; revised manuscript received 31 March 2019; published 17 May 2019)

Atomically precise placement of dopants in Si permits creating substitutional P nanowires by design. High-resolution images show that these wires are a few atoms wide with some positioning disorder with respect to the substitutional Si structure sites. Disorder is expected to lead to electronic localization in one-dimensional (1D)-like structures. Experiments, however, report good transport properties in quasi-1D P nanoribbons. We investigate theoretically their electronic properties using an effective single-particle approach based on a linear combination of donor orbitals (LCDO), with a basis of six orbitals per donor site, thus keeping the ground state donor orbitals' oscillatory behavior due to interference among the states at the Si conduction band minima. Our model for the P positioning errors accounts for the presently achievable placement precision allowing us to study the localization crossover. In addition, we show that a gatelike potential may control its conductance and localization length, suggesting the possible use of Si:P nanostructures as elements of quantum devices, such as nanoswitches and nanowires.

DOI: 10.1103/PhysRevB.99.205422

I. INTRODUCTION

The approaching breakdown of Moore's law has triggered a strong research effort to avoid compromising the miniaturization spiral in electronics. One of the promising strategies to keep it evolving consists in transferring current device functionalities to nanostructures prepared with atomic-scale control. Given the ubiquity of silicon integrated circuits presently in use, atomic implantation of dopants in Si hosts constitutes a very attractive road towards achieving such structures. This requires effective control of donor positioning at preassigned sites, i.e., fabricating devices at the atomic level by design [1–3]. Reports of successful placement of P arrays in Si suggest that this arrangement could, in principle, play the role of nanowires connecting different components of nanodevices, similar to a metallic wire in regular chips [1–7].

The adequacy of P nanochains and nanoribbons in Si to serve as channels for electronic transport in devices raises some questions. In principle, a perfectly ordered array does provide the desired connections [1–7]. However, in real samples the positioning uncertainties, inherent to the current fabrication processing standards, may spoil the desired conductance features: Due to the well known property that electronic states in disordered one-dimensional (1D) materials are localized [8], disordered nanowires can become insulators, with negligible electronic transport. Since the nanowires of interest here are finite, the electronic conductance is significant, as long as the electronic localization length is comparable to or larger than the system length itself [9].

Here we investigate these questions theoretically, modeling P nanochains and nanoribbons by a tight-binding description with six orbitals per P substitutional site, corresponding to the combinations of the six minima in the Si conduction band, symmetrized according to the tetrahedral crystal field potential at the donor site, see the Appendix. The sixfold degenerate levels split into states that have the symmetry of the different irreducible representations of the T_d group [10]. This leads to a singlet with A_1 symmetry, a triplet with T_2 symmetry, and a doublet with E symmetry. Starting from an ideal target configuration for the P sites, the actual positions are individually chosen according to a Gaussian distribution of lattice positions centered at each target site.

In this multiorbital scenario, we systematically study how the choice of the device geometry, namely the interdonor distance and the wire dimensions (width and length), affect the system's electronic conductance and localization. In addition, we show that such generated nanostructures can serve as nanoswitches controlled by an external gate potential.

This paper is organized as follows: In Sec. II we summarize the theoretical LCDO scheme, the atomistic model considered here, and the Landauer-Büttiker approach for quantum coherent transport. In Sec. III we outline the localization length calculation scheme and compare the main features of the different disorder intensities scenarios. In Sec. IV we investigate the sensitivity of the localization length parameter to an external gate potential and in Sec. V we analyze the corresponding effects on the nanostructure conductance. Our conclusions and summary are presented in Sec. VI.

II. MODEL AND METHODS

The full set of electronic states that describe mesoscopic nanostructures formed by donors in a Si host correspond to a Hilbert space whose size is typically larger than 10^6 atomic orbitals. As demonstrated in Refs. [9,11], the Hilbert space

---

[*] amintor.dusko@gmail.com

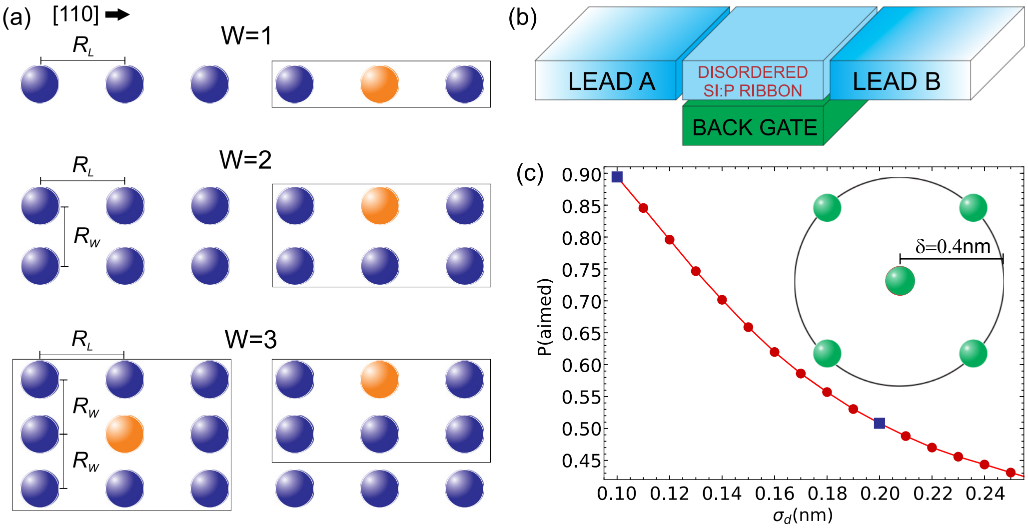

FIG. 1. (a) Target Si:P nanostructure fragment, along the Si [110] crystalline direction, for different widths W, specifying the geometric parameters R_W and R_L. The rectangles define a neighboring region around a reference site (orange sphere). The number of neighbors sites changes with W. For $W > 2$ one can define edge and bulk sites, with five and eight neighbors, respectively. (b) Sketch of the model system: disordered Si:P sample connected to semi-infinite leads with translational symmetry, subjected to a back gate potential. (c) Probability distribution P of an implanted donor to occupy the aimed position as a function of σ_d. Two cases are studied in this paper (blue squares): $\sigma_d = 0.1$ and 0.2 nm, corresponding to a deposition matching the aimed position 90% and 50% of the time, respectively. Inset: Graphical representation of the disorder cutoff radius δ. Here green spheres indicate the Si structure and the red circled sphere is the target position.

can be effectively represented by a reduced basis formed by a linear combination of donor orbital (LCDO). In this hybrid method each donor orbital is accounted for by a multivalley central cell effective mass approach that incorporates the Si host effects in the donor orbital itself.

We characterize the nanostructures by four geometric parameters, namely width (W), length (L), transversal donor distance (R_W), and longitudinal donor distance (R_L), see Fig. 1(a). Considering the placement process to occur along the Si $\langle 110\rangle$ direction, the target P donors form a rectangular lattice with lattice parameters defined by R_W and R_L.

The model multiorbital Hamiltonian written in the LCDO basis [9] reads

$$H = \sum_{i,l} \varepsilon_{i,l} n_{i,l} + \sum_{\langle i,j\rangle,l,m} t_{(i,l)(j,m)} c^{+}_{i,l} c_{j,m}, \qquad (1)$$

where $c^{+}_{i,l}$ ($c_{i,l}$) are creation (annihilation) operators of electrons at the orbital l centered at the ith site, $n_{i,l} = c^{+}_{i,l} c_{i,l}$ is the corresponding number operator, $\varepsilon_{i,l}$ is the onsite energy, and $t_{(i,l)(j,m)}$ the hopping term. In this equation $\langle i, j\rangle$ comprises the sum over pairs of sites for which the hopping terms are not negligible: The summation is performed over sites inside rectangular regions like the ones in Fig. 1(a). For $W = 1$, 2, and 3 we take up to two, five, and eight neighbors, respectively. The parameters were calculated within the LCDO scheme. In order to improve the reliability of the electronic calculations at smaller interdonor distances, we extend the treatment presented in Ref. [11] by including multiorbitals and three-center corrections due to neighboring cores in the hopping energies. A detailed presentation is found in the Appendix. These developments allow us to accurately address the nanoribbon model ($W \geqslant 2$ sites) placement parameters (R_L and R_W) of the order of 3 nm. We keep the isotropic approximation.

The model system we study consists of a central region, corresponding to the disordered Si:P nanostructure coupled to leads in thermal and chemical equilibrium with electronic reservoirs, see Fig. 1(b). The leads are semi-infinite, translational invariant, and define the electronic bands density of states coupled to the system of interest [12]. In addition, we investigate the effect of a uniform back gate potential and study its applicability to control the nanostructure transport properties. The gate potential V_G is included in the model as a correction to the onsite energy, namely, $\varepsilon_{i,l}(V_G) = \varepsilon_{i,l}(0) + U_G$. Here U_G is the shift in the electronic states energy and $\varepsilon_{i,l}(0)$ is the unbiased onsite energy calculated within the LCDO scheme. The energy gained by the electron is $U_G = \eta e V_G \propto -V_G$, where V_G is the gate potential, e is the electron charge, and η is a sample-dependent constant incorporating the Si dielectric screening, geometry, and the capacitive coupling of the donor electron with other leads in the system. We expect that some trends for a lateral gate potential as the one present in Refs. [2,3] can be inferred by comparing different nanoribbon widths, as a confining lateral potential decreases the effective W.

For sufficiently large values of V_G one expects that higher orbitals (such as $2p$ orbitals) influence the results. We estimate the validity of our approach as follows: Previous calculations [13] show that the lower energy states of a single donor remain in the A_1, T_2, E symmetry manifold. Remarkably, the corresponding energy levels remain almost constant up to a field strength of about 20 keV/cm, which are within the order of magnitude required to generate the U_G values we discuss.

We study the impact of positional disorder in such systems using a Gaussian disorder model. The disorder is quantified by two parameters, namely a cutoff radius δ[14] around a target substitutional site and the position standard deviation σ_d. For simplicity, we choose $\delta = 0.4\,\text{nm}$, in which case each donor can be placed at five different Si sites. The degree of disorder is controlled by σ_d. Figure 1(c) gives the dependence of the distribution of the implanted ion positions on σ_d. The main panel shows the probability distribution P of an implanted donor to occupy the aimed position as a function of σ_d and the inset gives a graphical representation of the disorder cutoff radius δ. The σ_d values considered in this work, namely $\sigma_d = 0.1\,\text{nm}$ and $\sigma_d = 0.2\,\text{nm}$, are indicated by the blue squares. These values are within state-of-the-art precision of STM atomic placement techniques [1,6,7].

We calculate the nanostructure linear conductance using the Landauer-Büttiker formula [15],

$$\mathcal{G}_{AB} = \frac{2e^2}{h}\int_{-\infty}^{\infty} dE\left(-\frac{\partial f}{\partial E}\right)T_{AB}(E), \tag{2}$$

given in terms of the Fermi-Dirac distribution function $f(E) = [1 + e^{(E-\mu)/k_BT}]^{-1}$ and the electronic transmission $T_{AB}(E) = \text{tr}[\mathbf{\Gamma}_B(E)\mathbf{G}^r(E)\mathbf{\Gamma}_A(E)\mathbf{G}^a(E)]$ [16]. In Eq. (2), $\mathbf{G}^r(\mathbf{G}^a)$ is the retarded (advanced) Green's function of the complete system (nanoribbon and leads), which we compute using the recursive Green's function approach, implemented as in Refs. [12,17,18]. The nth line or decay width, matrix elements $\mathbf{\Gamma}_n = i[\mathbf{\Sigma}_n^r - (\mathbf{\Sigma}_n^r)^\dagger]$, are obtained from the embedding self-energy $\mathbf{\Sigma}_n^r = \mathbf{V}_n^\dagger\mathbf{G}_n^r\mathbf{V}_n$, where $\mathbf{V}_n$ contains the coupling matrix elements of the sample with the nth lead, while $\mathbf{G}_n^r$ is the contact Green's function. There are several ways to calculate the latter [19–22]; we compute $\mathbf{G}_n^r$ by a standard decimation procedure based on renormalization-group ideas [23,24].

We cast the nanostructures transport properties in terms of the localization length ξ, formally defined by the wave function asymptotic behavior, $\Psi(x) \propto \exp(-|x|/\xi)$. In this work, we infer the localization length by the analysis of the conductance at zero temperature.

III. TRANSPORT AND PLACEMENT

Si:P nanostructures are multipath systems due to their multiorbital nature. The hopping term in this multiorbital framework plays an extremely nontrivial role, opening and closing channels depending on the system parameters. To improve the understanding of such a system towards applications in nanodevices control, we investigate how the disorder and placement parameters affect conductance and localization.

According to the localization theory in disordered systems [25], the conductance is expected to decrease exponentially with the ratio between the sample length L and the localization length ξ. Hence, we extract ξ from the relation $\langle \ln \mathcal{G}_{AB}(L)\rangle \propto -L/\xi$, where $\langle \ldots \rangle$ is an ensemble average [25] (here typically over $10^3 \ldots 10^4$ realizations). For each set of parameters, our algorithm selects iteratively a range of system lengths, from the order of 10^1 to 10^2 sites, to accurately determine the localization length ξ from the linear dependence of $\langle \ln \mathcal{G}_{AB}(L)\rangle$ with L. Figure 2 shows few representative examples of $\langle \ln \mathcal{G}_{AB}\rangle$ versus L and the corresponding linear fit that gives ξ.

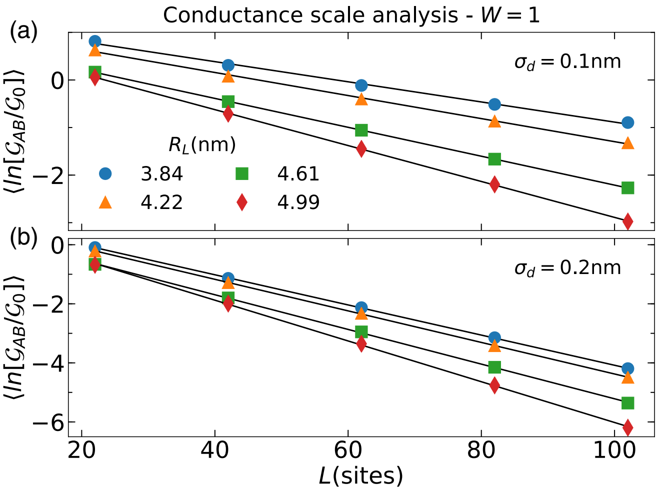

FIG. 2. Conductance $\mathcal{G}$ (in units of $\mathcal{G}_0 = 2e^2/h$) for disordered nanochains ($W = 1$) as a function of the system length L (in units of R_L or sites) for a few representative target interdonor distances R_L for (a) $\sigma_d = 0.1$ nm and (b) $\sigma_d = 0.2$ nm. The results correspond to an average over 10^4 disorder realizations. In all cases the standard deviations are smaller than the markers.

In Fig. 3 we present the localization length for $W = 1$ (nanochains) behavior with R_L for two levels of disorder. As expected, increasing R_L or the disorder level lowers ξ. Note that for small R_L we observe an enhanced sensitivity of ξ with σ_d. For these two disorder levels, ξ shows an abrupt fall around $R_L = 5.7\,\text{nm}$.

In order to represent the combined effect of the geometric parameters R_L and R_W in the transport trends of our system, we calculate the localization length $\xi(R_L, R_W)$ for $3.0\,\text{nm} \lesssim [R_L, R_W] \lesssim 6.5\,\text{nm}$. The range of values was chosen to represent realistic geometries of the current experimental realizations [1–3]. For technical reasons, our analysis is limited $R_W, R_L \gtrsim 3\,\text{nm}$, as discussed in the Appendix.

Figure 4 presents ξ as a function of R_L and R_W, where for each pair of parameters, ξ is represented by the given color code. In Figs. 4(a) and 4(b) we show $\xi(R_L, R_W)$ for disorder $\sigma_d = 0.1\,\text{nm}$ and in Figs. 4(c) and 4(d) for $\sigma_d = 0.2\,\text{nm}$. The frames on the left refer to $W = 2$ and on the

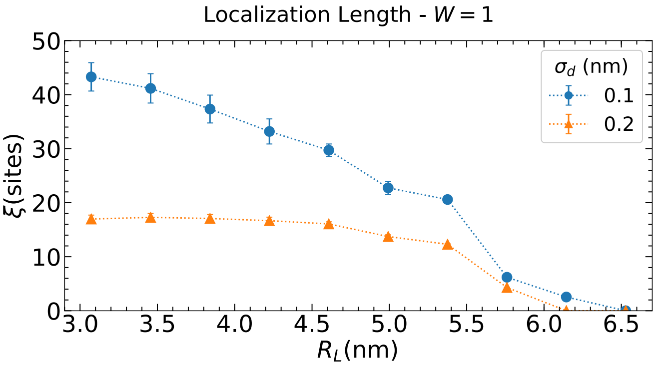

FIG. 3. Localization length ξ (in units of R_L or sites) as a function of the interdonor target separation R_L for nanochains ($W = 1$) and disorder intensities $\sigma_d = 0.1$ and 0.2 nm.

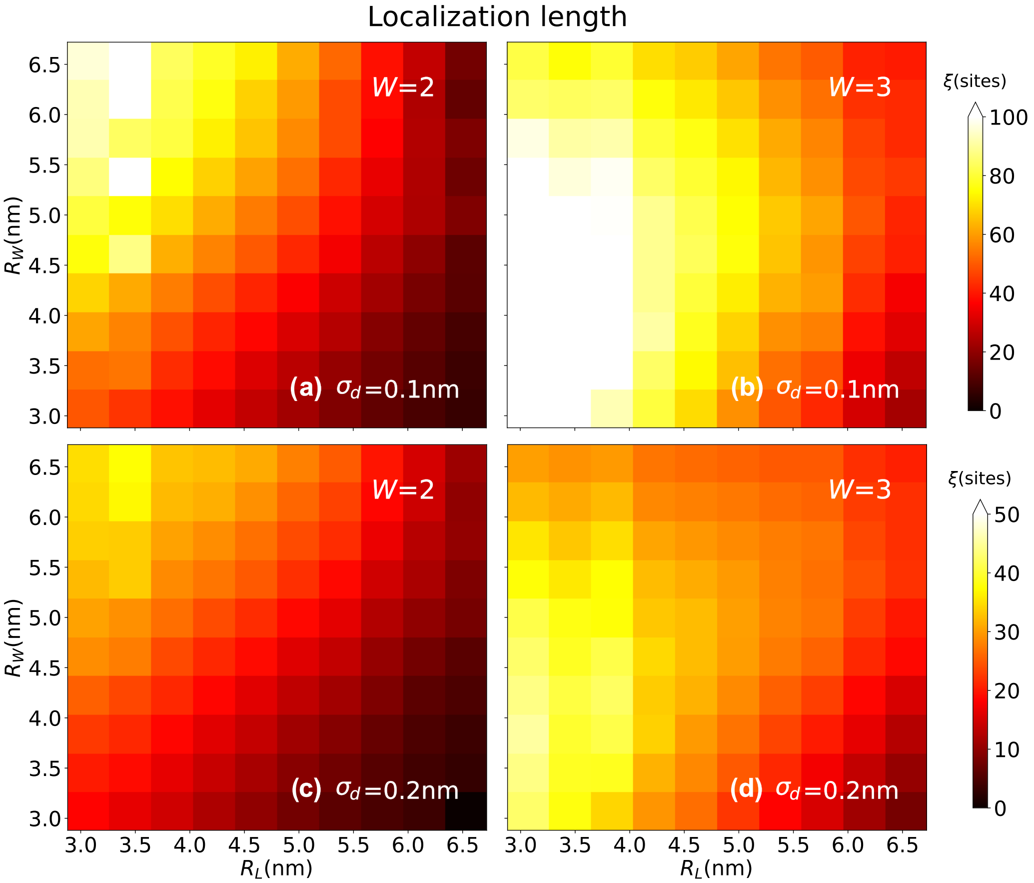

FIG. 4. Localization length ξ for nanoribbons of $W = 2$ and 3 as a function of the interdonor target separation R_L and R_W. Graphs with the same σ_d present the same color bar. (a) $\sigma_d = 0.1$ nm and $W = 2$, (b) $\sigma_d = 0.1$ nm and $W = 3$, (c) $\sigma_d = 0.2$ nm and $W = 2$, and (d) $\sigma_d = 0.2$ nm and $W = 3$.

right to $W = 3$. The results suggest a metal-insulator phase diagram with a very similar overall behavior for both disorder intensities presented. In Figs. 4(a) and 4(c) our simulations reveal a relatively small region in the investigated parameter space with nonmonotonic behavior, roughly $R_W \gtrsim 4.5$ nm and $R_L \lesssim 5.0$ nm. In particular, ξ is peaked at $R_L \approx 3.5$ nm and $R_W \approx 5.4,\ 6.1$, and 6.5 nm. Outside this nontrivial region, by increasing R_L or decreasing R_W the electronic states tend to become more localized. In Figs. 4(b) and 4(d) we find an overall increase of ξ and a wider region with nontrivial extended states, corresponding to the parameter range defined by $R_W \lesssim 6.0$ nm and $R_L \lesssim 4.2$ nm. In particular, ξ shows peaks for $R_L \approx 3.5$ nm and $R_W \approx 5.4$, 6.1, and 6.5 nm. Out of this nontrivial region, increasing R_L or decreasing R_W favors localization.

Comparing $W = 1,\ 2$, and 3 we observe an overall increasing in localization length with the system width, consistent with the increasing in the maximum number of transport channels, respectively, 6, 12, and 18. The sensitivity of ξ on the disorder intensity seems to become stronger for larger values of W.

IV. TUNING LOCALIZATION LENGTH

The nonmonotonic behavior of the localization length with the lattice geometry, namely R_L and R_W, suggests that one can tune it and hence control the system's conductance $\mathcal{G}$ by a suitable external handle. In what follows we show that a back gate potential, as described in Sec. II, is capable of dramatically modifying the transport properties of disordered Si:P nanowires. We recall that for electrons, $U_G \propto -V_G$.

In order to get some insight on the gate control over localization lengths in nanoribbons, we start with the nanowire case, $W = 1$. Results for ξ under a gate bias from 0 down to -250 meV are presented in Fig. 5 for two degrees of disorder. For a fixed interdonor distance, according to the smaller (larger) degree of disorder ξ oscillates in a larger (smaller) range in the graph truncated to 100 (50) nm. This nontrivial interference driven oscillatory behavior can be explained as follows: V_G rigidly shifts the nanowire energy spectrum. Hence, V_G drives localized and extended states, as well as small and large density of states of the disordered system across the Fermi energy fixed by the contacts. Given that the P donor in Si lower energy levels are 45 meV below the bottom of the Si conduction band edges, applying a bias of $U_G = 45$ meV would ionize the donors completely inside the active (sample) region. A wider range of control is provided for negative values of U_G which increases separation of the P electrons levels to the Si conduction band edge, thus remaining operational for the wide U_G range shown in the figures. Therefore we restrict our results to $U_G < 0\,(V_G > 0)$. The parameter range for a conducting behavior ($\xi/L \gtrsim 1$)

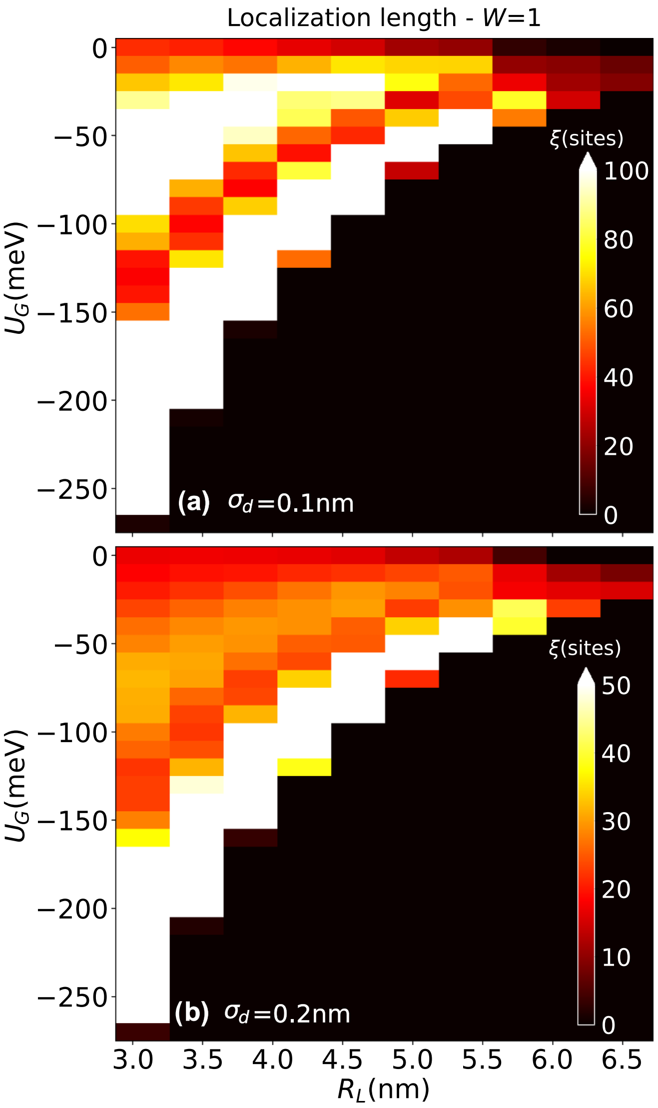

FIG. 5. Localization length ξ for nanochains ($W = 1$) as a function of the gate energy U_G and the interdonor target separation R_L for (a) $\sigma_d = 0.1$ nm and (b) $\sigma_d = 0.2$ nm.

shrinks for increasing values of R_L, consistent with the drop in the mean value of the hopping matrix elements.

The case $W = 2$ and $\sigma_d = 0.1$ nm is illustrated in Fig. 6. The simulations indicate an overall increase of ξ as a function of U_G followed by an oscillatory pattern. As in the $W = 1$ case we observe that the U_G range corresponding to conducting behavior shrinks with R_L. In addition, a similar feature can be observed for increasing values of R_W. By varying U_G for different R_W values, we find the formation of a gap—a region of negligible values of ξ—followed by a "reactivation" in the localization phase diagram for larger values of R_L. This gap is highlighted in Figs. 6(a)–6(c) where the threshold R_L values are 4.6 nm, 5 nm, and 5.4 nm, respectively. The gap R_L threshold value continues to increase monotonically along Figs. 6(d)–6(f). In the last three panels [Figs. 6(g)–6(i)], the gap closes resembling the signature of the $W = 1$ case. Although it is reasonable to recover a phase diagram similar to $W = 1$ case while increasing R_W, we observe an enhancement in the overall localization length values and V_G range leading to conducting behavior.

The wider ribbon case, $W = 3$, is given in Fig. 7. As in $W = 1$ and 2 cases, one observes an increase in ξ with U_G followed by an oscillatory pattern and that the U_G range leading to conducting behavior shrinks with R_L and R_W interdonor distances. For smaller R_W values, Figs. 7(a)–7(c) show a larger gap than in the $W = 2$ case and the opening of a second gap. Throughout Figs. 7(d)–7(f) we observe that this second gap is short lived compared to the first one. In summary, we find that both ξ and U_G range leading to conducting behavior are overall larger than in the $W = 1$ and 2 cases. We have also performed calculations for $\sigma_d = 0.2$ nm, for both $W = 2$ and 3, not shown since all properties follow the trends identified in the previous cases.

V. CONDUCTANCE CONTROL

In this section, we investigate the use of a gate potential V_G ($U_G \propto -V_G$) as an external control of conductance $\mathcal{G}_{AB}$ for Si:P nanostructures. Here we set $L = 60$ sites for the purpose of investigating a nanoswitch implementation in a length comparable to the experimental realizations [1–3] of higher P density.

Figure 8 shows the average conductance $\mathcal{G}_{AB}$ as a function of U_G and R_L for nanochains ($W = 1$). The results show oscillations in $\mathcal{G}_{AB}$ as a function of both R_L and V_G. A minimum in $\mathcal{G}_{AB}$ occurs around $R_L \approx 4.6$ nm, which should be avoided in practical implementations of the system as a nanoswitch. Oscillations due to U_G stand out for smaller R_L values. In line with the localization length analysis, an increase of R_L causes the range of U_G values corresponding to a conducting behavior to shrink. For $R_L \approx 3.1$ nm, introducing a gate potential, we observe an increase in $\mathcal{G}_{AB}$ of approximately 50% and 100% for $\sigma_d = 0.1$ nm and 0.2 nm, respectively.

The conductance for $W = 2$ sites nanoribbons and $\sigma_d = 0.1$ nm results, presented in Fig. 9, show a rapidly oscillatory behavior as a function of U_G for small R_W values, see Figs. 9(a) and 9(b). For larger R_W values however [see Figs. 9(e) and 9(f)] the oscillations are strongly damped for small U_G. In all cases, it is possible to observe a U_G transition edge between larger and smaller $\mathcal{G}_{AB}$ values regimes. There is also a minimum in $\mathcal{G}_{AB}$ around $R_L \approx 3.5$ nm; the feature is more pronounced in the cases shown in Figs. 9(b)–9(e). We observe a very subtle gap opening in $\mathcal{G}_{AB}$ while increasing R_L. The R_L value corresponding to this opening increases with R_W. In Figs. 9(a), 9(c) and 9(e) the corresponding gapping opening value is $R_L \approx 4.2$, 5.0, and 5.4 nm, respectively. As in the $W = 1$ case, introducing a gate potential induces an increase of approximately 50% in $\mathcal{G}_{AB}$.

The results for nanoribbons of $W = 3$ sites are presented in Fig. 10. Some similarities with $W = 2$ case can be observed: Rapidly oscillating $\mathcal{G}_{AB}$ spectrum with a clear change in overall behavior in a given transition edge, for an example see Fig. 10(a) at $R_L \approx 3.1$ nm and $U_G = -350$ meV. In contrast with the $W = 2$ case we observe two gap openings and an overall minimum in $\mathcal{G}_{AB}$ values around $R_L \approx 3.9$ nm. The first gap can be observed in Figs. 10(a), 10(c) and 10(e) for $R_L \approx 5.0$, 5.4, and 5.9 nm, respectively. The second gap is more

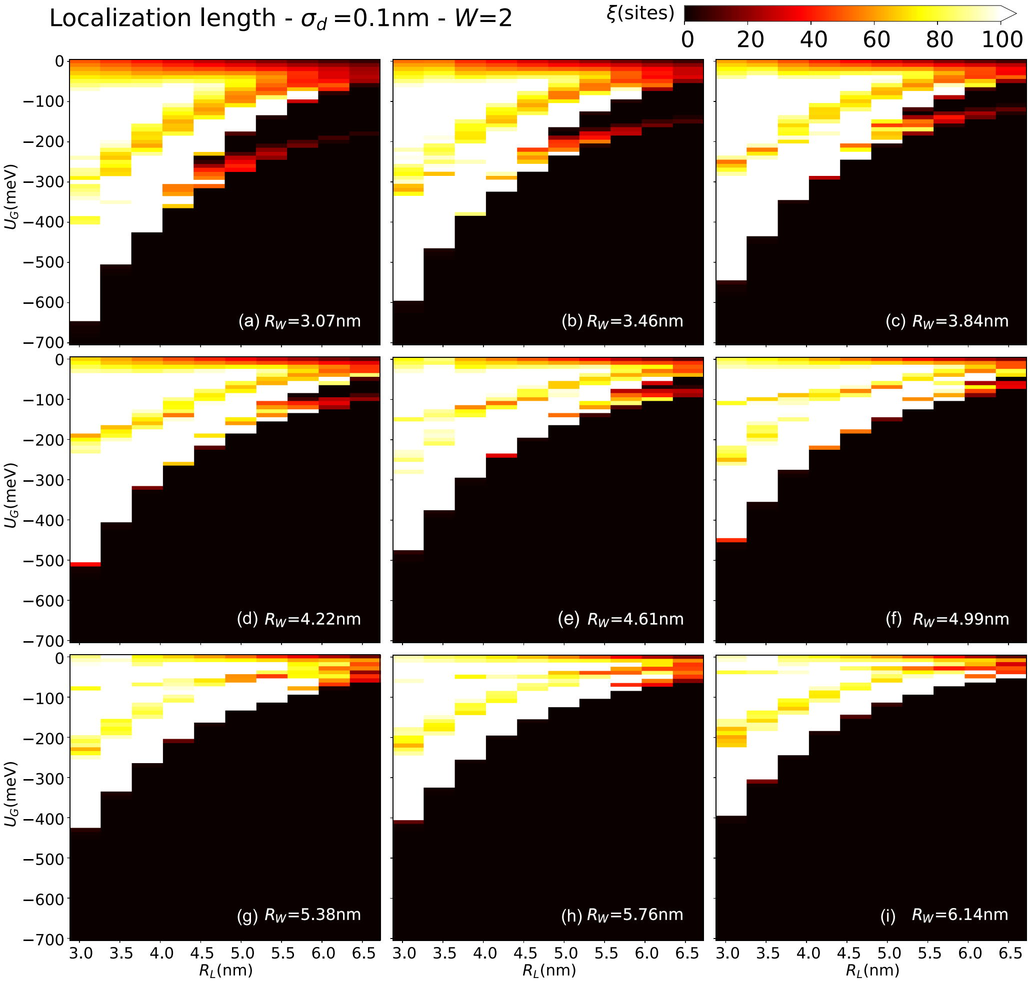

FIG. 6. Localization length ξ as a function of V_G and R_L (R_W fixed) for nanoribbons of $W = 2$ and $\sigma_d = 0.1$ nm. (a)–(i) correspond to different values of R_W.

subtle but can be observed in Fig. 10(d) for $R_L \approx 5.9$ nm, for example.

In summary, by considering nanostructures with increasing width, $W = 1,\ 2$, and 3, we observe a corresponding increase in: (i) the overall $\mathcal{G}_{AB}$ values, (ii) the window of V_G values leading to a conducting behavior, and (iii) in the number of gap openings. We also observe a change in the R_L value corresponding to an overall minimum in $\mathcal{G}_{AB}$. We also find that the overall behavior of the conductance on the lattice parameters does not depend on the disorder strength. This can be explicitly seen for the $W = 1$ case by comparing the simulations for $\sigma_d = 0.2$ nm and 0.1 nm.

Finally, let us stress the sharp V_G driven metal-insulator transition appearing for any given choice of R_L in all cases we analyze in this work. This remarkable feature strongly suggests that Si:P nanostructures can act as switches by properly tuning the gate potential.

VI. DISCUSSIONS AND CONCLUSIONS

In this work we extended the LCDO formalism [9,11] to include Gaussian disorder, a multiorbital description, and technical improvements, specified in the Appendix, which results in a more realistic description of P nanochains and to access nanoribbons of arbitrary widths. Our simulations treat the problem considering realistic system sizes and disorder. We also have put forward a proposal for an external control of transport properties such as localization length and conductance suggesting a new path of investigations for future experimental implementations.

We have found nontrivial features of the electronic transport properties due to system fabrication specifications still remaining robust against disorder. Specific values of placement parameters and nanostructure width provide optimized localization length, favoring high conductance. Our calculations indicate that a similar behavior is expected for different disorder levels.

We further analyze the effects of an external back gate potential V_G to localization length and conductance. Properly tuning V_G one can control localization lengths, allowing donor nanowires to keep current-carrying wave functions even for relatively long samples, serving as efficient connectors among nanodevices parts. In addition, it is possible to increase the nanostructure conductance, or decrease it by using this external potential, which suggests the use of such structures as nanoswitches. Both connectors and switches provide state-

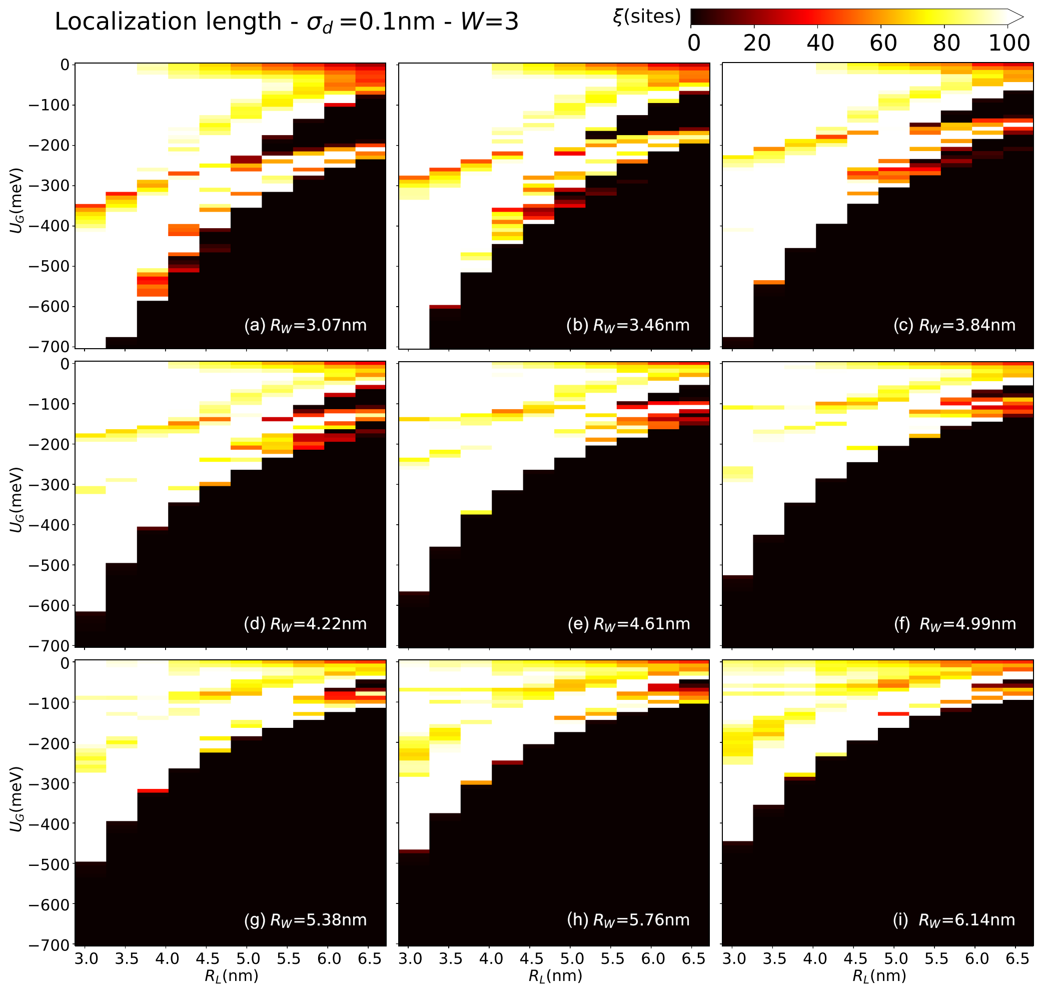

FIG. 7. Localization length ξ as a function of V_G and R_L (R_W fixed) for nanoribbons of $W = 3$ and $\sigma_d = 0.1$ nm. (a)–(i) correspond to different values of R_W.

of-the-art resources contributing to nanodevices technology development.

ACKNOWLEDGMENTS

The authors acknowledge the financial support of the Brazilian funding agencies CL CNPq (Grant No. 308801/2015-6) and FAPERJ (Grant No. E-26/202.882/2018); BK CNPq (Grant No. 304869/2014-7) and FAPERJ (Grant No. E-26/202.767/2018). This study was also financed in part by the Coordenação de Aperfeiçoamento de Pessoal de Nível Superior - Brazil (CAPES) - Finance Code 001.

APPENDIX: MICROSCOPIC MODEL—TECHNICAL DETAILS

The multiorbital approach employed in this study represents a significant generalization of the method used in our previous works, where only one A_1 orbital per site was considered [9,11]. Here, effects due to neighboring donor potentials, known to change the ground-state symmetry for small interdonor distances, are correctly treated. Nonetheless, the first order perturbation theory breaks down for sufficiently small values of the interdonor distances R_L and R_W. We estimate the lower bound to be around 3 nm.

1. Linear Combination of Dopant Orbitals (LCDO)

Following the well established Kohn and Luttinger prescription [10,26,27] for shallow donors in Si, we consider a basis of six donor orbitals per site, corresponding to the six minima in Si conduction band. Valley orbit coupling, included by first order perturbation theory for degenerate states [28,29], renders donor orbitals as superpositions of pure valley states obtained by the effective mass approach:

$$\Psi_i^l(\mathbf{r}) = \frac{1}{N_l}\sum_{\mu=1}^{6} a_\mu^l F_\mu(\mathbf{r}-\mathbf{R}_i)\phi_\mu(\mathbf{r}-\mathbf{R}_i), \tag{A1}$$

where l refer to the donor i orbitals pinned to the donor coordinates $\mathbf{R}_i$. The constants N_l and a_μ^l stand for the normalization and valley population (presented in Table I), $F_\mu(\mathbf{r}) = F(r) = (\pi a^{*3})^{-1/2} e^{-r/a^*}$ is for simplicity approximated as an isotropic hydrogenlike envelope function, with a species dependent effective Bohr radius a^* (1.106 nm for Si:P), and $\phi_\mu(\mathbf{r}) = e^{ik_\mu\cdot\mathbf{r}}u_\mu(\mathbf{r})$ are the Bloch functions of the six Si conduction band degenerate minima ($\mu = 1,\ldots,6$). The latter

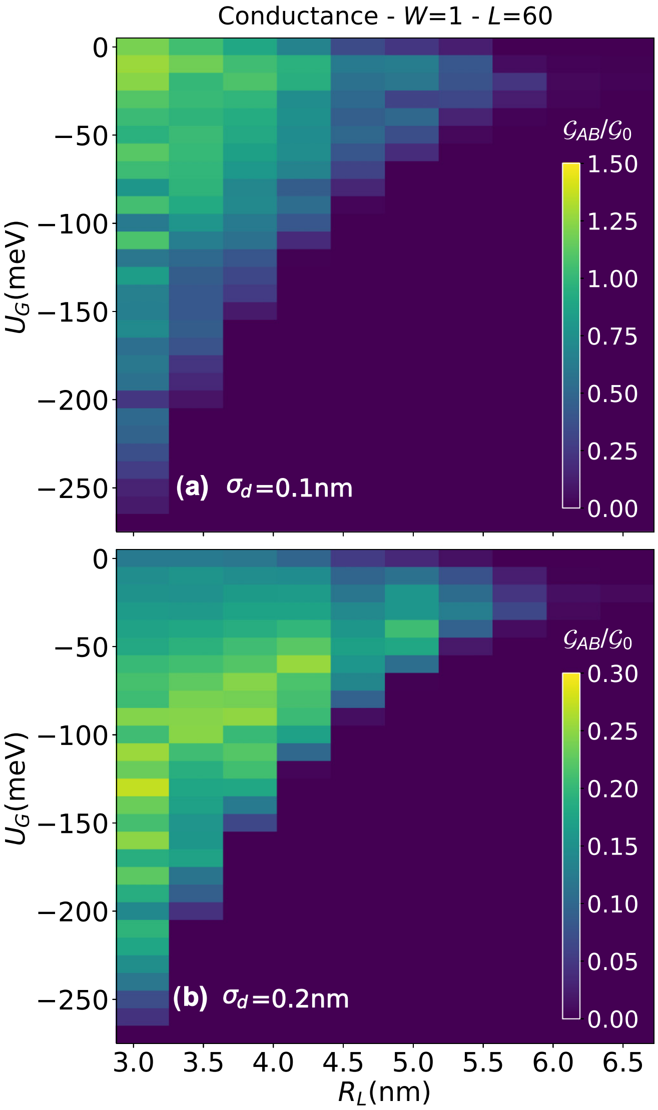

FIG. 8. Conductance $\mathcal{G}_{AB}$ (in units of $\mathcal{G}_0 = 2e^2/h$) as a function of a gate potential V_G and interdonor target separation R_L for nanochains ($W = 1$), $L = 60$ sites, and (a) $\sigma_d = 0.1$ nm, (b) $\sigma_d = 0.2$ nm.

are located along the equivalent directions $\pm x$, $\pm y$, $\pm z$ at $|\mathbf{k}_\mu| = k_0 = 0.85(2\pi/a_{\text{Si}})$, where a_{Si} is the conventionally called Si lattice parameter [30]. The effective Bohr radius is obtained by incorporating screening effects due to the Si host charge carriers in the donor singular potential.

Screening effects are included through a potential that interpolates the expected behavior for large and small values of r, namely,

$$V(r) = -\frac{e^2}{4\pi r}\left[\frac{1}{\epsilon_{\text{Si}}} + \left(\frac{1}{\epsilon_0} - \frac{1}{\epsilon_{\text{Si}}}\right)e^{-r/r^*}\right], \tag{A2}$$

the screening length r^* defines the transition between a bare $V(r \to 0) = -e^2/4\pi\epsilon_0 r$ and a screened $V(r \to \infty) = -e^2/4\pi\epsilon_{\text{Si}} r$ potential. Here ϵ_0 and ϵ_{Si} are, respectively, the free space and the static relative permittivities.

As in previous works [9,11] the Hamiltonian terms are calculated by the atomistic Hamiltonian $\hat{H} = \hat{H}_i + \hat{H}'$, where $\hat{H}_i$ is the single donor Hamiltonian and $\hat{H}'$ is the perturbation due to neighboring donor cores. We project the donor orbital to this atomistic Hamiltonian to extract the onsite and hopping terms. For the onsite term we obtain,

$$\varepsilon_{i,l} = \langle i|\hat{H}_i|i\rangle + \langle i|\hat{H}'|i\rangle \approx -E_l + \sum_k \langle i|\hat{V}_k|i\rangle, \tag{A3}$$

where E_l is the single donor level energy given in Table I, which contains valley-orbit corrections.

Similarly the hopping reads,

$$t_{(i,l)(j,m)} = \langle j|\hat{H}_i|i\rangle + \langle j|\hat{H}'|i\rangle \tag{A4a}$$

$$\approx -E_0\langle j|i\rangle + \sum_k \langle j|\hat{V}_k|i\rangle = \mathcal{T}_{ij}(R)\Theta^{lm}(\mathbf{R})$$

$$\Theta^{lm} = \frac{1}{N_l N_m}\sum_{\mu,\nu=1}^{6} a^l_\mu a^m_\nu e^{i\mathbf{k}_\mu\cdot\mathbf{R}} \tag{A4b}$$

$$\mathcal{T}_{ij}(R) = E_0\mathcal{S}_{ij} + T_{ijj} + \sum_k T_{ikj} \tag{A4c}$$

$$\mathcal{S}_{ij}(R) = \langle F(\mathbf{R}_j)|F(\mathbf{R}_i)\rangle \tag{A4d}$$

$$T_{ikj} = \langle F(\mathbf{R}_j)|V(\mathbf{R}_k)|F(\mathbf{R}_i)\rangle, \tag{A4e}$$

where $\mathbf{R} = \mathbf{R}_j - \mathbf{R}_i$ is the interdonor distance, E_0 is the donor ground state energy, Θ^{lm} comes from the valley interference, and $\mathcal{T}_{ij}(R)$ depends on the envelope overlap function $\mathcal{S}_{ij}$ and on two-centers (T_{ijj}) and three-centers (T_{ikj}) envelope function integrals. The T_{ijj} integrals have a closed analytical solution [11], while the T_{ikj} are calculated numerically. The k labels all cores in the neighborhood of the i and j donors, see Fig. 1(a).

Comparisons with experiments show that this multivalley central cell corrected dopant approximation gives an accurate description of the single impurity spectrum [29] and the corresponding wave functions [31], as well as the two impurities spectra in ionized [32] and neutral excited states [33]. The computational advantage is clear: By incorporating the Si matrix explicitly in the orbitals, this approach allows the investigation of shallow donor systems of mesoscopic dimensions, a prohibitive task for a full atomistic approach.

2. Gaussian Expansion—Three-center Integrals

In this paper we consider hopping terms due to all neighboring cores. Since the straightforward calculation of these three-center integrals is computationally expensive, we write the envelope orbitals and the Coulomb potential, as a Gaussian expansion, namely

$$F(r) = \sum_{n=1}^{N_{\text{G}}} c^F_n e^{-s^F_n r^2}, \tag{A5}$$

$$V(r) = -\frac{e^2}{4\pi r}\left[\frac{1}{\epsilon_{\text{Si}}} + \left(\frac{1}{\epsilon_0} - \frac{1}{\epsilon_{\text{Si}}}\right)\sum_{n=1}^{N_{\text{G}}} c^V_n e^{-s^V_n r^2}\right], \tag{A6}$$

where the coefficients c^F_n, c^V_n, s^F_n, and s^V_n are obtained by a standard least square fit and presented in Table II. We find

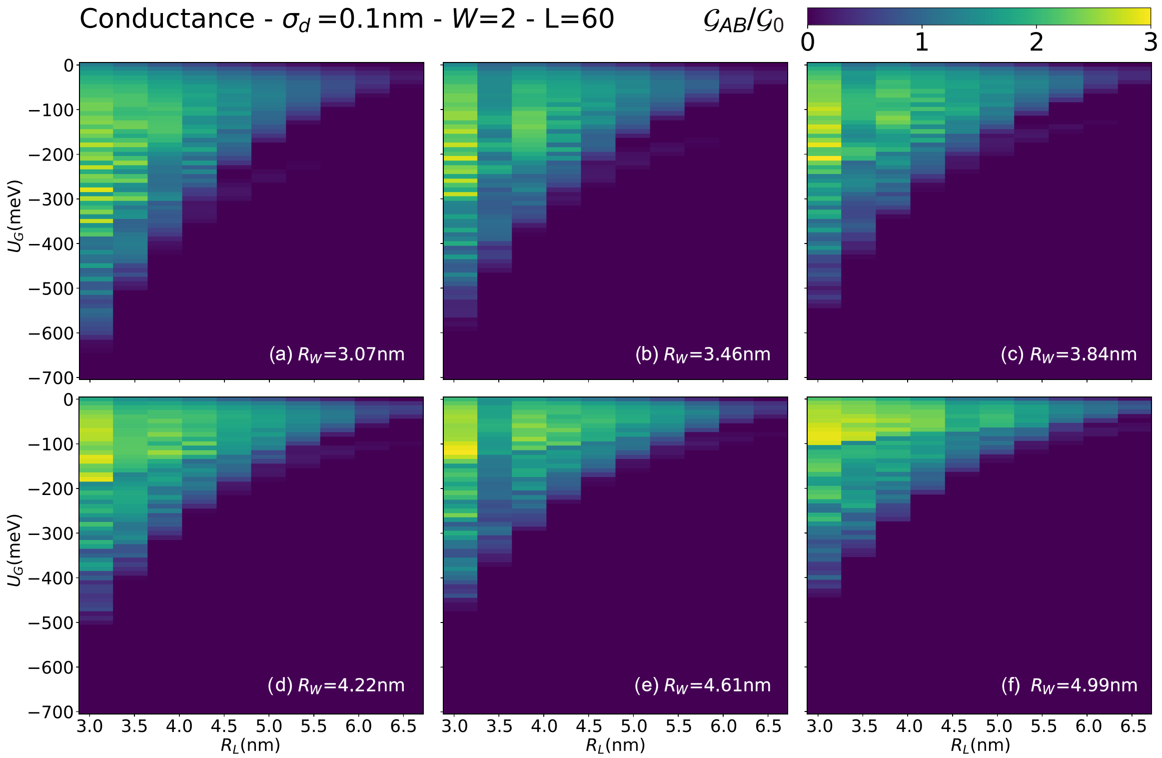

FIG. 9. Conductance $\mathcal{G}_{AB}$ (in units of $\mathcal{G}_0 = \frac{2e^2}{h}$) for disordered nanoribbons of $W = 2$ and $L = 60$ sites with $\sigma_d = 0.1$ nm as a function of a gate potential V_G and interdonor target separations R_L and R_W. (a)–(f) correspond to different values of R_W.

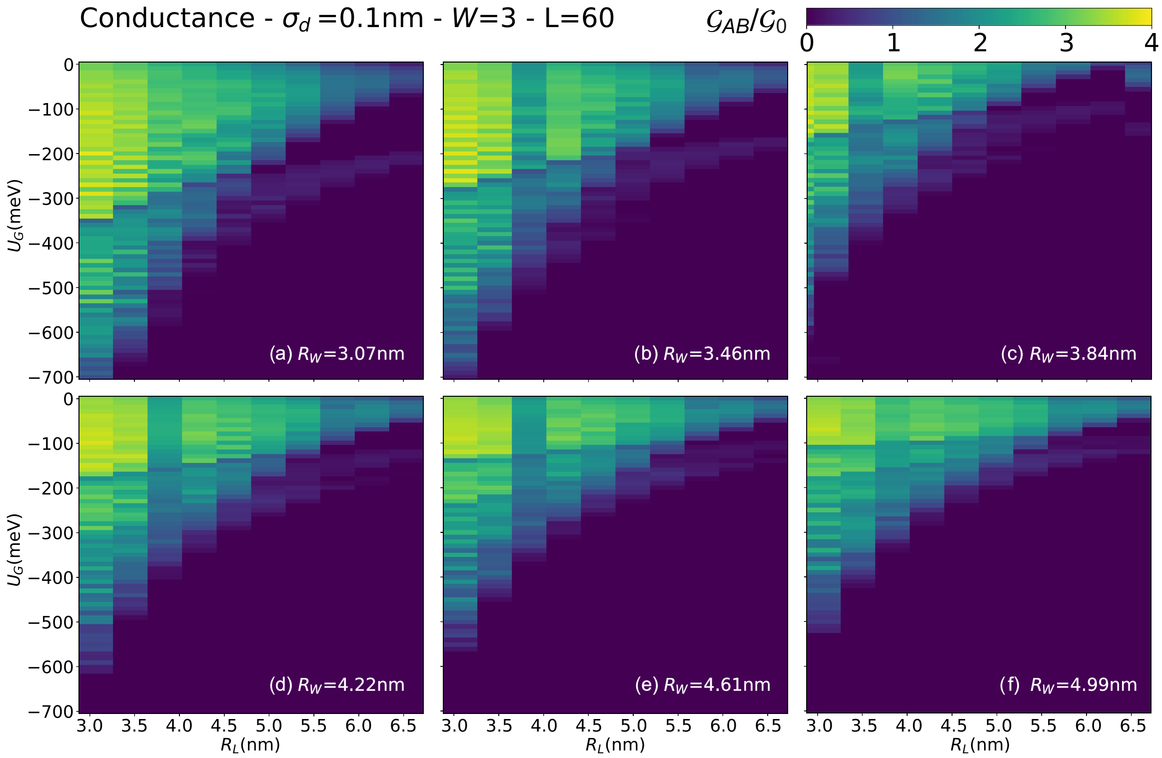

FIG. 10. Conductance $\mathcal{G}_{AB}$ (in units of $\mathcal{G}_0 = \frac{2e^2}{h}$) for nanoribbons of $W = 3$ and $L = 60$ sites with $\sigma_d = 0.1$ nm as a function of a gate potential V_G and interdonor target separations R_L and R_W. (a)–(f) correspond to different values of R_W.

TABLE I. Valley population a^l_μ, normalization constant N_l, and P^0 donor energy E_l for the six donor orbitals l.

l	a^l_x	a^l_{-x}	a^l_y	a^l_{-y}	a^l_z	a^l_{-z}	N_l	E_l (meV)
A$_1$	1	1	1	1	1	1	$\sqrt{6}$	−45.58
T$_2^z$	0	0	0	0	1	−1	$\sqrt{2}$	
T$_2^y$	0	0	1	−1	0	0	$\sqrt{2}$	−33.90
T$_2^x$	1	−1	0	0	0	0	$\sqrt{2}$	
E^{xy}	1	1	−1	−1	0	0	2	−32.60
E^z	1	1	1	1	−2	−2	$\sqrt{12}$	

that by taking $N_G = 13$ Gaussian terms, the expansions agree within 10^{-8} accuracy for all values of r where the target function satisfies $f(r) \gtrsim 10^{-20}$.

3. Gaussian Coulomb Integrals—Product Rule

Let us now show the main derivation steps to obtain very simple expressions for the Gaussian integrals introduced above. The Gaussian expansion of the Coulomb three-center integral T_{acb} reads

$$\begin{aligned} T_{acb} &= \langle F(\mathbf{R}_b)|V(\mathbf{R}_c)|F(\mathbf{R}_a)\rangle \\ &= \sum_{m,n} c^F_m c^F_n \int_V d\mathbf{r}\, e^{-s^F_m r_b^2} e^{-s^F_n r_a^2} V(\mathbf{r}_c), \end{aligned} \tag{A7}$$

where $r_n = |\mathbf{r} - \mathbf{R}_n|$ is the relative position to donor n.

Let us now use the Gaussian product rule, i.e.,

$$e^{-s^F_m r_b^2} e^{-s^F_n r_a^2} = e^{-\eta_{mn} R_{ba}^2} e^{-u_{mn} r_u^2}, \tag{A8}$$

where the constants $u_{mn} = s^F_m + s^F_n$ and $\eta_{mn} = s^F_m s^F_n / u_{mn}$ are the total and reduced exponents, while $R_{ba} = |\mathbf{R}_a - \mathbf{R}_b|$ and $r_u = (s^F_m r_b + s^F_n r_a)/u_{mn}$ are the relative and the Gaussian center of mass positions. Equation (A8) expresses the product of two Gaussians in a new product where the first term is a constant and only the second term depends on $\mathbf{r}$. In other words, the problem is reduced to a two-center integral

$$T_{acb} = \sum_{m,n} c^F_m c^F_n e^{-\eta_{mn} R_{ba}^2} \int_V d\mathbf{r}\, e^{-u_{mn} r_u^2} V(\mathbf{r}_c). \tag{A9}$$

When $V(\mathbf{r})$ is a screened Coulomb potential, this two-centers integral can be decomposed in two terms, i.e., $T_F(\mathbf{r}_u, \mathbf{r}_c) = T_{Si}(\mathbf{r}_u, \mathbf{r}_c) + T_{sc}(\mathbf{r}_u, \mathbf{r}_c)$. The Gaussian expansion of the exponential term in the $V(r)$ gives

$$T_{\rm Si} = -\frac{e^2}{4\pi\epsilon_{Si}} \sum_{m,n} c^F_m c^F_n e^{-\eta_{mn} R_{ba}^2} \mathcal{I}^{\rm Si}_{mn},$$

$$\mathcal{I}^{\rm Si}_{mn} = \int_V d\mathbf{r}\, e^{-u_{mn} r_u^2} \frac{1}{r_c},$$

$$T_{sc} = -\frac{e^2}{4\pi}\left(\frac{1}{\epsilon_0} - \frac{1}{\epsilon_{\rm Si}}\right) \sum_{m,n,o} c^F_m c^F_n c^V_o e^{-\eta_{mn} R_{ba}^2} \mathcal{I}^{sc}_{mno},$$

$$\mathcal{I}^{sc}_{mno} = \int_V d\mathbf{r}\, e^{-u_{mn} r_u^2} \frac{e^{-s^F_o r_c^2}}{r_c}.$$

The next step consists of writing r_c^{-1} as a Gaussian integral, namely, $r_c^{-1} = \pi^{-1/2} \int_{-\infty}^{\infty} dt\, e^{-t^2 r_c^2}$. After rearranging the integrals and applying the product rule in the sc term, one obtains

$$\mathcal{I}^{\rm Si}_{mn} = \frac{1}{\sqrt{\pi}} \int_{-\infty}^{\infty} dt \int_V d\mathbf{r}\, e^{-u_{mn} r_u^2} e^{-t^2 r_c^2},$$

$$\mathcal{I}^{sc}_{mno} = \frac{1}{\sqrt{\pi}} e^{-\nu_{mno} R_{uc}^2} \int_{-\infty}^{\infty} dt \int_V d\mathbf{r}\, e^{-\upsilon_{mno} r_\upsilon^2} e^{-t^2 r_c^2},$$

where $\upsilon_{mno} = (u_{mn} + s^F_o)$, $\nu_{mno} = u_{mn} s^F_o / \upsilon_{mno}$, $R_{uc} = |\mathbf{R}_c - \mathbf{R}_u|$, and $r_\upsilon = |\mathbf{r} - \mathbf{R}_\upsilon|$ where $\mathbf{R}_\upsilon = (u_{mn}\mathbf{R}_u + s^F_o \mathbf{R}_c)/\upsilon_{mno}$. Applying the product rule, as in Eq. (A8), we find

$$\mathcal{I}^{\rm Si}_{mn} = \frac{1}{\sqrt{\pi}} \int_{-\infty}^{\infty} dt\, e^{-\left(\frac{u_{mn} t^2}{u_{mn}+t^2}\right) R_{uc}^2} \int_V d\mathbf{r}\, e^{-(u_{mn}+t^2) r_p^2}$$

where $r_p = (u_{mn} r_u + t^2 r_c)/(u_{mn} + t^2)$ and

$$\mathcal{I}^{sc}_{mno} = \frac{e^{-\nu_{mno} R_{uc}^2}}{\sqrt{\pi}} \int_{-\infty}^{\infty} dt\, e^{-\left(\frac{\upsilon_{mno} t^2}{\upsilon_{mno}+t^2}\right) R_{\upsilon c}^2} \int_V d\mathbf{r}\, e^{-(\upsilon_{mno}+t^2) r_q^2}$$

where $r_q = (\upsilon_{mno} r_\upsilon + t^2 r_c)/(\upsilon_{mno} + t^2)$ and $R_{\upsilon c} = |\mathbf{R}_c - \mathbf{R}_\upsilon|$. As in Eq. (A8), the spatial integrals depend only on the Gaussian center of mass r_p and r_q.

Finally, adjusting the integration limit in the remaining integrals, we obtain the simple expressions

$$\mathcal{I}^{\rm Si}_{mn} = \frac{2}{\sqrt{\pi}} \int_0^{\infty} \left(\frac{\pi}{u_{mn} + t^2}\right)^{3/2} e^{-\left(\frac{u_{mn} t^2}{u_{mn}+t^2}\right) R_{uc}^2} dt,$$

$$\mathcal{I}^{sc}_{mno} = \frac{2e^{-\nu_{mno} R_{uc}^2}}{\sqrt{\pi}} \int_0^{\infty} dt \left(\frac{\pi}{\upsilon_{mno} + t^2}\right)^{3/2} e^{-\left(\frac{\upsilon_{mno} t^2}{\upsilon_{mno}+t^2}\right) R_{\upsilon c}^2}.$$

By introducing the change of variables $q_u^2 = t^2/(u_{mn} + t^2)$ and $q_\upsilon^2 = t^2/(\upsilon_{mno} + t^2)$ the integrals are conveniently written as

$$\begin{aligned} \mathcal{I}^{\rm Si}_{mn} &= 2\pi \int_0^1 dq_u\, e^{-u_{mn} R_{uc} q_u^2} = 2\pi F_0\big[u_{mn} R_{uc}^2\big], \\ \mathcal{I}^{sc}_{mno} &= 2\pi e^{-\nu_{mno} R_{uc}^2} \int_0^1 dq_\upsilon\, e^{-\upsilon_{mn} R_{\upsilon c} q_\upsilon^2} \\ &= 2\pi e^{-\nu_{mno} R_{uc}^2} F_0\big[\upsilon_{mn} R_{\upsilon c}^2\big], \end{aligned} \tag{A10}$$

TABLE II. Gaussian expansion coefficients for the envelope function $F(r)$ and exponential in the screened Coulomb potential $V(r)$.

$F(r)$		$V(r)$	
c^F_n	s^F_n (nm^{-2})	c^V_n	s^V_n (nm^{-2})
9.26×10^{-2}	4.10×10^{-1}	1.91×10^{-1}	3.82×10^{1}
8.56×10^{-2}	9.19×10^{-1}	1.76×10^{-1}	8.60×10^{1}
7.31×10^{-2}	1.89×10^{-1}	1.52×10^{-1}	1.76×10^{1}
6.71×10^{-2}	2.15	1.38×10^{-1}	2.02×10^{2}
4.80×10^{-2}	5.30	9.86×10^{-2}	4.99×10^{2}
3.26×10^{-2}	1.38×10^{1}	6.68×10^{-2}	1.31×10^{3}
3.13×10^{-2}	8.99×10^{-2}	6.53×10^{-2}	8.35
2.12×10^{-2}	3.89×10^{1}	4.34×10^{-2}	3.70×10^{3}
1.33×10^{-2}	1.20×10^{2}	2.72×10^{-2}	1.15×10^{4}
8.03×10^{-3}	4.20×10^{2}	1.63×10^{-2}	4.05×10^{4}
4.68×10^{-3}	1.78×10^{2}	9.47×10^{-3}	1.74×10^{5}
3.84×10^{-3}	4.26×10^{-2}	8.03×10^{-3}	3.96
3.73×10^{-3}	1.54×10^{4}	7.45×10^{-3}	1.53×10^{6}

where F_0 is called zero degree Boys function [34,35]. To optimize computational resources we choose to solve the integral once, with high precision and in a range covering small and large values, and to adjust a curve that interpolates with rapidly decaying exponentials the expected behavior in all domains.

$$F_0^{\mathrm{adj}}(x) = e^{-s_1 x^6} \sum_{n=0}^{6} B_n x^n + \left(1 - e^{-s_2 x^6}\right) \frac{1}{2} \sqrt{\frac{\pi}{x}} \qquad \text{(A11)}$$

The coefficients of the fitted curve are presented in Table III. For the domain we considered, $x \in [10^{-8}, 10^4]$, we find that $|F_0^{\mathrm{adj}} - F_0| \approx 10^{-7}$, confirming the fitting quality.

TABLE III. Fitting coefficients of Boys function, see Eq. (A11).

Coefficient	Fitted value
s_1	6.70×10^{-5}
B_0	1.00
B_1	-3.33×10^{-1}
B_2	9.94×10^{-2}
B_3	-2.28×10^{-2}
B_4	3.81×10^{-3}
B_5	-3.99×10^{-4}
B_6	2.15×10^{-5}
s_2	6.01×10^{-5}

---

[1] B. Weber, S. Mahapatra, H. Ryu, S. Lee, A. Fuhrer, T. C. G. Reusch, D. Thompson, W. C. T. Lee, G. Klimeck, L. C. L. Hollenberg, and M. Y. Simmons, Science **335**, 64 (2012).

[2] B. Weber, H. Ryu, Y.-H. Matthias Tan, G. Klimeck, and M. Y. Simmons, Phys. Rev. Lett. **113**, 246802 (2014).

[3] S. Shamim, B. Weber, D. W. Thompson, M. Y. Simmons, and A. Ghosh, Nano Lett. **16**, 5779 (2016).

[4] S. R. Schofield, N. J. Curson, M. Y. Simmons, F. J. Rueß, T. Hallam, L. Oberbeck, and R. G. Clark, Phys. Rev. Lett. **91**, 136104 (2003).

[5] M. Fuechsle, J. A. Miwa, S. Mahapatra, H. Ryu, S. Lee, O. Warschkow, L. C. L. Hollenberg, G. Klimeck, and M. Y. Simmons, Nat. Nanotechnol. **7**, 242 (2012).

[6] F. A. Zwanenburg, A. S. Dzurak, A. Morello, M. Y. Simmons, L. C. L. Hollenberg, G. Klimeck, S. Rogge, S. N. Coppersmith, and M. A. Eriksson, Rev. Mod. Phys. **85**, 961 (2013).

[7] J. Salfi, J. A. Mol, R. Rahman, G. Klimeck, M. Y. Simmons, L. C. L. Hollenberg, and S. Rogge, Nat. Commun. **7**, 11342 (2016).

[8] T. Brandes and S. Kettemann, (eds.) *Anderson Localization and Its Ramifications: Disorder, Phase Coherence, and Electron Correlations* (Springer Verlag, Berlin, 2003).

[9] A. Dusko, A. L. Saraiva, and B. Koiller, Phys. Rev. B **94**, 115425 (2016).

[10] W. Kohn, *Shallow Impurity States in Silicon and Germanium*, edited by F. Seitz and D. Turnbull, Solid State Physics Vol. 5 (Academic Press, New York, 1957), pp. 257–320.

[11] A. Dusko, A. Delgado, A. Saraiva, and B. Koiller, npj Quantum Inf. **4**, 1 (2018), for details on the LCDO formalism see the Supplemental Material.

[12] C. H. Lewenkopf and E. R. Mucciolo, J. Comput. Electron. **12**, 203 (2013).

[13] A. Debernardi, A. Baldereschi, and M. Fanciulli, Phys. Rev. B **74**, 035202 (2006).

[14] The cutoff radius has been introduced to avoid unphysical inversions in the ordering of donor positioning along the array. For realistic values of σ the effect of the cutoff radius on the reported results is almost negligible. For instance, for $\sigma = 0.1$ nm with a cutoff radius we preserve 99.99% of the samples.

[15] S. Datta, *Electronic Transport in Mesoscopic Systems* (Cambridge University Press, Cambridge, 1997).

[16] Y. Meir and N. S. Wingreen, Phys. Rev. Lett. **68**, 2512 (1992).

[17] E. Ridolfi, L. R. F. Lima, E. R. Mucciolo, and C. H. Lewenkopf, Phys. Rev. B **95**, 035430 (2017).

[18] L. R. F. Lima, A. Dusko, and C. Lewenkopf, Phys. Rev. B **97**, 165405 (2018).

[19] M. P. Lopez Sancho, J. M. Lopez Sancho, and J. Rubio, J. Phys. F: Met. Phys. **15**, 851 (1985).

[20] A. MacKinnon, Z. Phys. B **59**, 385 (1985).

[21] A. R. Rocha, V. M. García-Suárez, S. Bailey, C. Lambert, J. Ferrer, and S. Sanvito, Phys. Rev. B **73**, 085414 (2006).

[22] M. Wimmer, Quantum transport in nanostructures: From computational concepts to spintronics in graphene and magnetic tunnel junctions, Ph.D. thesis, University Regensburg (2009).

[23] C. E. T. G. da Silva and B. Koiller, Solid State Commun. **40**, 215 (1981).

[24] M. O. Robbins and B. Koiller, Phys. Rev. B **27**, 7703 (1983).

[25] P. Sheng, *Introduction to Wave Scattering, Localization and Mesoscopic Phenomena* (Springer-Verlag Berlin Heidelberg, Heidelberg, 2006).

[26] J. M. Luttinger and W. Kohn, Phys. Rev. **97**, 869 (1955).

[27] W. Kohn and J. M. Luttinger, Phys. Rev. **98**, 915 (1955).

[28] B. Koiller, X. Hu, and S. Das Sarma, Phys. Rev. B **66**, 115201 (2002).

[29] A. L. Saraiva, A. Baena, M. J. Calderón, and B. Koiller, J. Phys.: Condens. Matter **27**, 154208 (2015).

[30] O. Madelung, *Semiconductors: Data Handbook* (Springer Science & Business Media, Berlin, 2012).

[31] A. L. Saraiva, J. Salfi, J. Bocquel, B. Voisin, S. Rogge, R. B. Capaz, M. J. Calderón, and B. Koiller, Phys. Rev. B **93**, 045303 (2016).

[32] M. F. Gonzalez-Zalba, A. Saraiva, M. J. Calderón, D. Heiss, B. Koiller, and A. J. Ferguson, Nano Lett. **14**, 5672 (2014).

[33] J. P. Dehollain, J. T. Muhonen, K. Y. Tan, A. Saraiva, D. N. Jamieson, A. S. Dzurak, and A. Morello, Phys. Rev. Lett. **112**, 236801 (2014).

[34] S. Boys, Proc. Roy. Soc. **200**, 542 (1950).

[35] P. M. W. Gill, Adv. Quantum Chem. **25**, 141 (1994).